molecules

MDPI

Article

Insights into the Understanding of the Nickel-Based Pre-Catalyst Effect on Urea Oxidation Reaction Activity

Haipeng Liu [1,2], Peike Wang [1,2], Xue Qi [1,2], Ao Yin [1,2], Yuxin Wang [1,2], Yang Ye [1,2], Jingjing Luo [1,2], Zhongqi Ren [1,2], Lina Chen [1,2,*], Suzhu Yu [1,2,*] and Jun Wei [1,2,3,*]

1 Shenzhen Key Laboratory of Flexible Printed Electronics Technology, Harbin Institute of Technology (Shenzhen), Shenzhen 518055, China; ddxd_lhp@163.com (H.L.); 22s155067@stu.hit.edu.cn (P.W.); qixue@hit.edu.cn (X.Q.); yinao505@outlook.com (A.Y.); yxwang202104@126.com (Y.W.); 21s155114@stu.hit.edu.cn (Y.Y.); 21b355005@stu.hit.edu.cn (J.L.); zhong_qi_ren@163.com (Z.R.)
2 School of Materials Science and Engineering, Harbin Institute of Technology (Shenzhen), Shenzhen 518055, China
3 State Key Laboratory of Advanced Welding and Joining, Harbin Institute of Technology (Shenzhen), Shenzhen 518055, China
* Correspondence: linachen@hit.edu.cn (L.C.); szyu@hit.edu.cn (S.Y.); junwei@hit.edu.cn (J.W.)

Abstract: Nickel-based catalysts are regarded as the most excellent urea oxidation reaction (UOR) catalysts in alkaline media. Whatever kind of nickel-based catalysts is utilized to catalyze UOR, it is widely believed that the in situ-formed Ni^{3+} moieties are the true active sites and the as-utilized nickel-based catalysts just serve as pre-catalysts. Digging the pre-catalyst effect on the activity of Ni^{3+} moieties helps to better design nickel-based catalysts. Herein, five different anions of OH^-, CO_3^{2-}, SiO_3^{2-}, MoO_4^{2-}, and WO_4^{2-} were used to bond with Ni^{2+} to fabricate the pre-catalysts β-$Ni(OH)_2$, Ni-CO_3, Ni-SiO_3, Ni-MoO_4, and Ni-WO_4. It is found that the true active sites of the five as-fabricated catalysts are the same in situ-formed Ni^{3+} moieties and the five as-fabricated catalysts demonstrate different UOR activity. Although the as-synthesized five catalysts just serve as the pre-catalysts, they determine the quantity of active sites and activity per active site, thus determining the catalytic activity of the catalysts. Among the five catalysts, the amorphous nickel tungstate exhibits the most superior activity per active site and can catalyze UOR to reach 158.10 mA·cm^{-2} at 1.6 V, exceeding the majority of catalysts. This work makes for a deeper understanding of the pre-catalyst effect on UOR activity and helps to better design nickel-based UOR catalysts.

Keywords: urea oxidation reaction; pre-catalyst; quantity of active sites; activity per active site

check for updates

Citation: Liu, H.; Wang, P.; Qi, X.; Yin, A.; Wang, Y.; Ye, Y.; Luo, J.; Ren, Z.; Chen, L.; Yu, S.; et al. Insights into the Understanding of the Nickel-Based Pre-Catalyst Effect on Urea Oxidation Reaction Activity. *Molecules* **2024**, *29*, 3321. https://doi.org/10.3390/molecules29143321

Academic Editor: Guiyong Xiao

Received: 24 June 2024
Revised: 9 July 2024
Accepted: 12 July 2024
Published: 15 July 2024

Copyright: © 2024 by the authors. Licensee MDPI, Basel, Switzerland. This article is an open access article distributed under the terms and conditions of the Creative Commons Attribution (CC BY) license (https://creativecommons.org/licenses/by/4.0/).

1. Introduction

Substituting renewable energies for fossil fuels is an effective method to conquer energy and environment problems at the same time, which is an urgent need for our society [1–6]. However, renewable energies like solar and wind have drawbacks such as intermittency and transportation difficulties. Water electrolysis powered by renewable energies can transform these renewable energies into hydrogen molecules which can solve the drawbacks of renewable energies [7–12]. Water electrolysis is composed of the hydrogen evolution reaction (HER) at the anode and oxygen evolution reaction (OER) at the cathode [13–15]. Compared with HER, OER makes up the majority of energy waste in water electrolysis due to the inherent sluggish kinetics [16–20]. Changing the OER by the urea oxidation reaction (UOR) can extremely decrease the overpotential of overall water electrolysis, thus improving the utilization of renewable energies [1,3,10,19,20]. Therefore, the design of cheap and efficient UOR catalysts has received much attention from scientists.

Since the discovery of urea electrolysis, platinum and rhodium have been regarded as the most superior UOR catalysts [21]. The rare reserves and high cost of platinum and rhodium prompt the scientists to design new catalysts. Nickel-based catalysts bio-inspired

from urease have received much attention since their discovery and they exhibit comparable UOR performance to precious metals platinum and rhodium [7,22–25]. In order to obtain more active nickel-based catalysts, various types of nickel-based catalysts were developed to catalyze UOR mainly spanning from nickel oxides [17,24,26–30], nickel X-ides (X refers to C, N, P, S, Se, Te, etc.) [3,11,22,25,31], nickel-based composites [9,23,32], etc. For nickel oxide-related catalysts, Chen's group added Rh nanoparticles to NiO nanosheets which outperformed the counter NiO nanosheets [27]. Rh and NiO are both UOR active components, and the addition of Rh nanoparticles endows the NiO nanosheet with a superior electronic structure. For nickel X-ide-related catalysts, Zhang's group supported nickel nitride nanospheres on nickel foam, which can efficiently catalyze the hydrogen generation and urea decomposition [31]. The superior electron conductivity of the support nickel foam brought out the catalytic performance of nickel nitride. For nickel-based composite-related catalysts, Hameed's group developed a type of NiO/graphene composite by a facile coprecipitation and calcination method [33]. The introduction of graphene improves the conductivity of NiO and alters the electronic structure of NiO, and the NiO/graphene composite demonstrates more enhanced UOR activity than NiO. Through lots of in situ experimental research by advanced instruments and many theoretical investigations, although various types of nickel-based UOR catalysts are synthesized and demonstrate different UOR performances, it is widely believed that the as-synthesized catalysts just serve as the pre-catalysts and the in situ-formed Ni^{3+} moieties are the true active sites [24,25,34]. Since the true active sites are all Ni^{3+} moieties, we question why different nickel-based catalysts demonstrate different UOR activity and what the significance of synthesizing different types of nickel-based catalysts is Systematic investigation about the effect of pre-catalysts on UOR activity helps to understand the meaning of synthesizing different kinds of catalysts and will lay a great foundation for further enhancing the UOR performance of nickel-based catalysts.

In this work, five catalysts were synthesized by bonding Ni^{2+} with OH^-, CO_3^{2-}, SiO_3^{2-}, MoO_4^{2-} and WO_4^{2-} anions, respectively. Modern characterization techniques were adopted to analyze the catalyst structure and lots of electrochemical methods were utilized to uncover the UOR mechanism. It is found that the as-fabricated five catalysts just serve as the pre-catalysts and the true active sites are the in situ-formed Ni^{3+} moieties. The pre-catalysts determine the UOR catalytic activity by deciding the quantity of active sites and activity per active site. The as-prepared amorphous nickel tungstate exhibits the most superior activity per active site and demonstrates superior UOR activity, selectivity, and durability. This work helps to better understand the UOR mechanism.

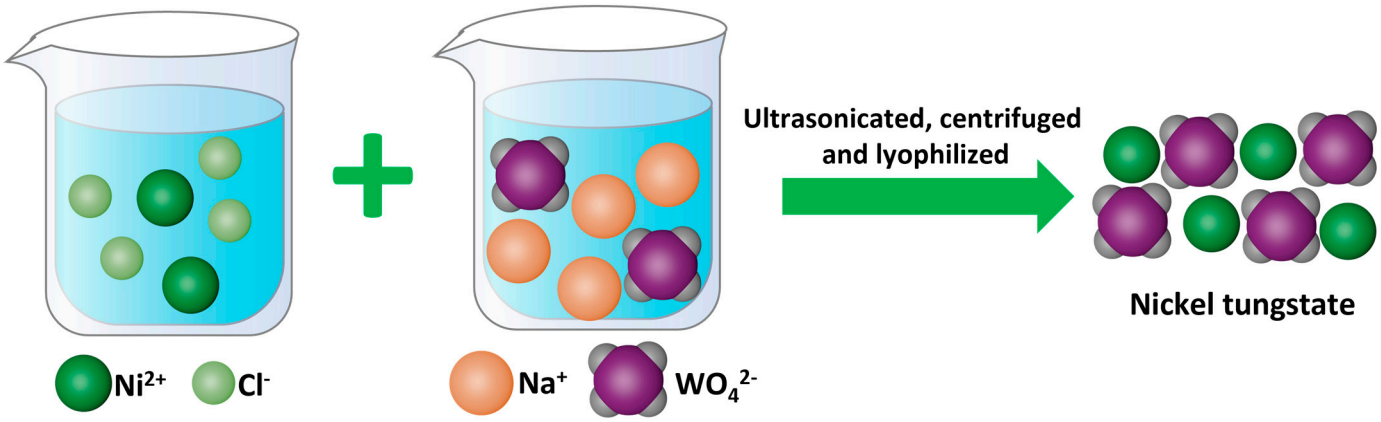
2. Results and Discussion

2.1. Structure Characterization

β-$Ni(OH)_2$, Ni-CO_3, Ni-SiO_3, Ni-MoO_4, and Ni-WO_4 catalysts were fabricated according to Scheme 1, which is detailed in the Materials and Methods section. β-$Ni(OH)_2$, Ni-CO_3, Ni-SiO_3, Ni-MoO_4, and Ni-WO_4 were obtained by mixing the Ni^{2+} solution with OH^-, CO_3^{2-}, SiO_3^{2-}, MoO_4^{2-}, and WO_4^{2-} solutions, respectively, followed by ultrasonication, centrifugation, and lyophilization.

XRD was adopted to analyze the catalyst structure shown in Figure S1. β-$Ni(OH)_2$ was poorly crystallized and typical peaks of (001), (100), and (011) facets located at 19.2, 33.2, and 38.6° were indexed to PDF#73–1520 [30]. XRD patterns of Ni-CO_3, Ni-SiO_3, Ni-MoO_4, and Ni-WO_4 all demonstrated amorphous hump peaks and the amorphous features were verified by their corresponding HRTEM images. TEM was used to observe the catalyst morphologies and analyze the detailed catalyst phase structure. β-$Ni(OH)_2$, Ni-CO_3, Ni-SiO_3, Ni-MoO_4, and Ni-WO_4 all display nanoparticle morphologies (Figures 1a and S2a–d). A (011) facet of 0.21 nm is observed in the HRTEM image of β-$Ni(OH)_2$ and the selected area electron diffraction (SAED) pattern demonstrates typical polycrystalline diffraction ring feature (Figure S2e) [32,35,36]. No lattice planes can be detected in the HRTEM images of Ni-CO_3, Ni-SiO_3, Ni-MoO_4, and Ni-WO_4, and their corresponding SAED patterns all

demonstrate amorphous halo features (Figures S2f–h and 1b). Uniform distribution of elements Ni, O, and W can be seen in the EDS mapping images of Ni-WO_4 and signals of Ni, O, and W are clearly detected in the EDS diagram of Ni-WO_4 (Figure 1c). XRD and TEM results illustrate that β-Ni$(OH)_2$ is a poorly crystallized nanoparticle, and Ni-CO_3, Ni-SiO_3, Ni-MoO_4, and Ni-WO_4 are amorphous nanoparticles.



Scheme 1. Synthetic scheme of Ni-WO_4.

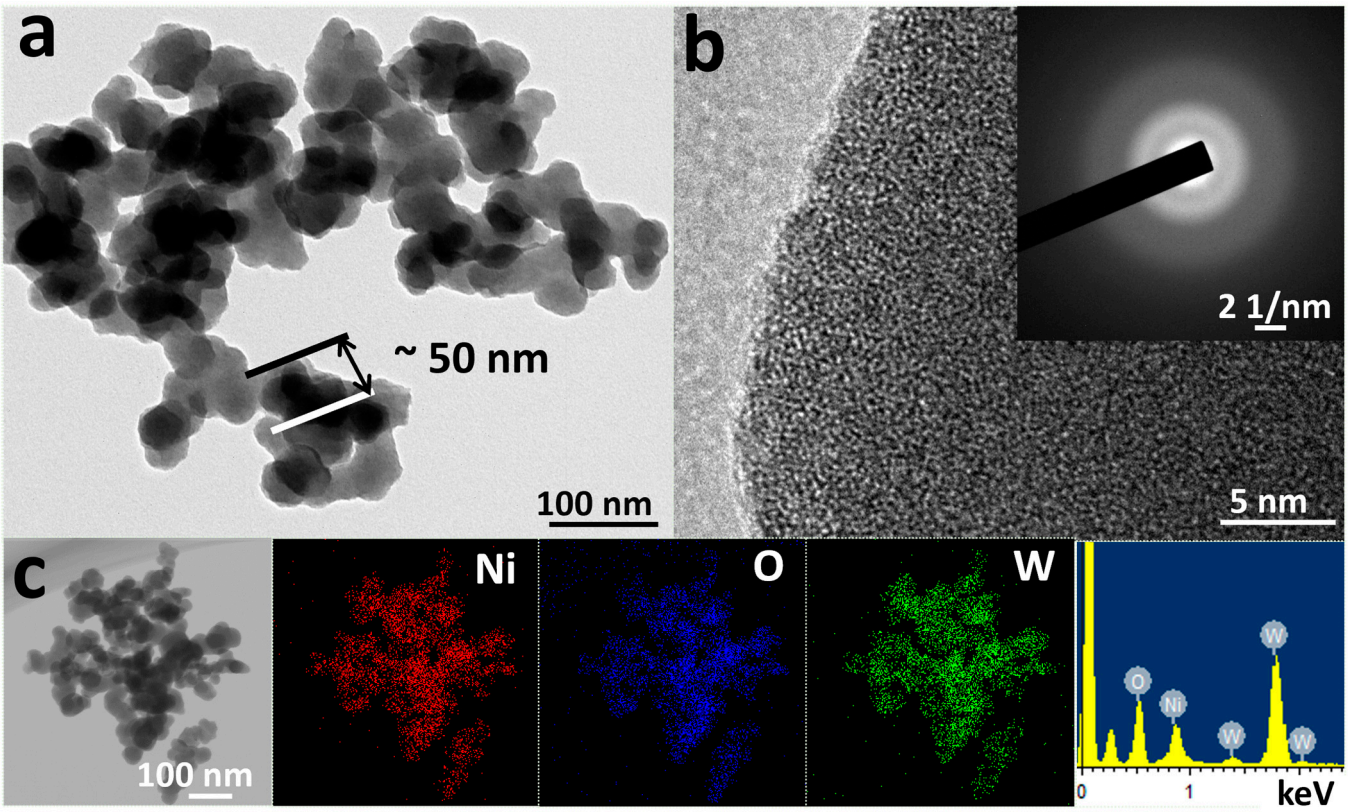


Figure 1. (**a**) TEM image, (**b**) HRTEM image, inset is SAED pattern, and (**c**) EDS mapping images and EDS diagram of Ni-WO_4.

Element chemical environments were characterized by XPS. Ni $2p_{3/2}$ XPS of β-Ni$(OH)_2$, Ni-CO_3, Ni-SiO_3, Ni-MoO_4, and Ni-WO_4 were fitted by the moiety of Ni^{2+} (856.10 eV), followed by a satellite (861.60 eV) at a higher binding energy (Figure 2a) [12,36,37]. The fittings of O 1s XPS are different (Figure 2b). C-O moieties (531.70 eV) and C=O moieties (533.00 eV) from adventitious carbon and OH^- moieties (530.85 eV) from β-Ni$(OH)_2$ structure were detected on β-Ni$(OH)_2$ [30,36]. C-O moieties (531.50 eV) and C=O moieties

(533.00 eV) from nickel carbonate structure were detected on Ni-CO_3 [36,38,39]. Si-O moieties (531.50 eV) and Si=O moieties (533.00 eV) from nickel metasilicate structure were detected on Ni-SiO_3 [40,41]. C-O moieties (531.70 eV) and C=O moieties (533.00 eV) from adventitious carbon and Mo-O moieties (530.31 eV) from nickel molybdate structures were detected on Ni-MoO_4 [42,43]. C-O moieties (531.70 eV) and C=O moieties (533.00 eV) from adventitious carbon and W-O moieties (530.31 eV) from nickel tungstate structures were detected on Ni-WO_4 [7,43]. Si $2p_{3/2}$ (102.45 eV) and $2p_{1/2}$ (103.06 eV) were detected on Ni-SiO_3 (Figure S3a) [41]. Mo $3d_{5/2}$ (232.13 eV) and $3d_{3/2}$ (235.26 eV) were detected on Ni-MoO_4 (Figure S3b) [42,44].

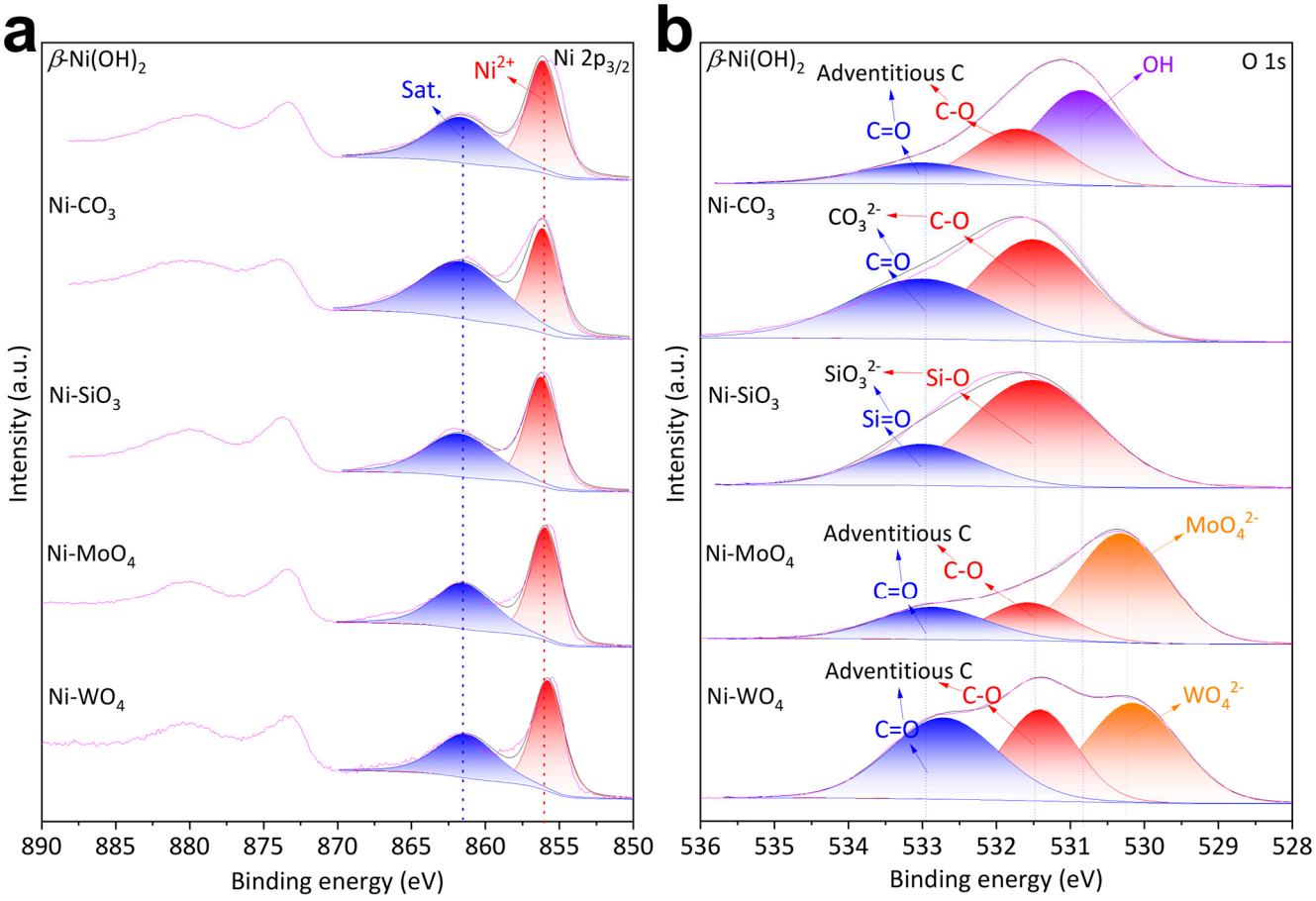


Figure 2. (**a**) Ni 2p XPS and (**b**) O 1s XPS of β-Ni$(OH)_2$, Ni-CO_3, Ni-SiO_3, Ni-MoO_4, and Ni-WO_4.

2.2. Electrochemical Analysis

Electrochemical measurements were conducted on electrochemical workstations. UOR CV curves of β-Ni$(OH)_2$, Ni-CO_3, Ni-SiO_3, Ni-MoO_4, and Ni-WO_4 all demonstrate a more negative overpotential than those of OER at a fixed current density, while 20 wt.% Ir/C does not (Figure S4a). Therefore, the as-fabricated five catalysts are all applicable to UOR catalysis. β-Ni$(OH)_2$, Ni-CO_3, Ni-SiO_3, Ni-MoO_4, and Ni-WO_4 start to catalyze UOR at a potential of 1.35, 1.34, 1.35, 1.35, and 1.36 V, respectively. β-Ni$(OH)_2$, Ni-CO_3, Ni-SiO_3, Ni-MoO_4, and Ni-WO_4 deliver 10 mA·cm^{-2} at 1.41, 1.39, 1.42, 1.38, and 1.38 V, respectively. β-Ni$(OH)_2$, Ni-CO_3, Ni-SiO_3, Ni-MoO_4, and Ni-WO_4 catalyze UOR at 1.6 V reaching 44.87, 117.69, 19.86, 112.60, and 158.10 mA·cm^{-2}, respectively. Onset potentials and overpotentials at 10 mA·cm^{-2} do not show significant differences. But Ni-WO_4 can catalyze UOR to reach an extremely higher current density at 1.6 V than β-Ni$(OH)_2$, Ni-CO_3, Ni-SiO_3, and Ni-MoO_4. UOR kinetics were examined by Tafel slope values. Ni-WO_4 exhibits a lower value of 39.8 mV·dec^{-1} than β-Ni$(OH)_2$ (64.6 mV·dec^{-1}), Ni-CO_3 (40.7 mV·dec^{-1}), Ni-SiO_3 (56.6 mV·dec^{-1}), and Ni-MoO_4 (40.2 mV·dec^{-1}) (Figure 3b). UOR selectivity was performed

on an RRDE equipment. The ring electrode demonstrates negligible current of the UOR RRDE curves, while the ring electrode exhibits obvious current of the OER RRDE curves, suggesting that O_2 was produced during the OER test and no O_2 was produced during the UOR test. Therefore, we can conclude that β-Ni(OH)$_2$, Ni-CO_3, Ni-SiO_3, Ni-MoO_4, and Ni-WO_4 can effectively oxidize urea molecules in the tested solution. The UOR stability of Ni-WO_4 was examined by the CP method. Ni-WO_4 can catalyze the UOR for at least 30 h at 10 mA·cm^{-2} (Figure 3d). Catalyst support can effectively impact the catalyst activity. Therefore, UOR activity of the as-fabricated five catalysts is compared to catalysts decorated on the same support in previous publications. Impressively, the UOR activity of Ni-WO_4 exceeds the majority of the superior catalysts (Figure 3e) [17,18,24–26,32,45–48].

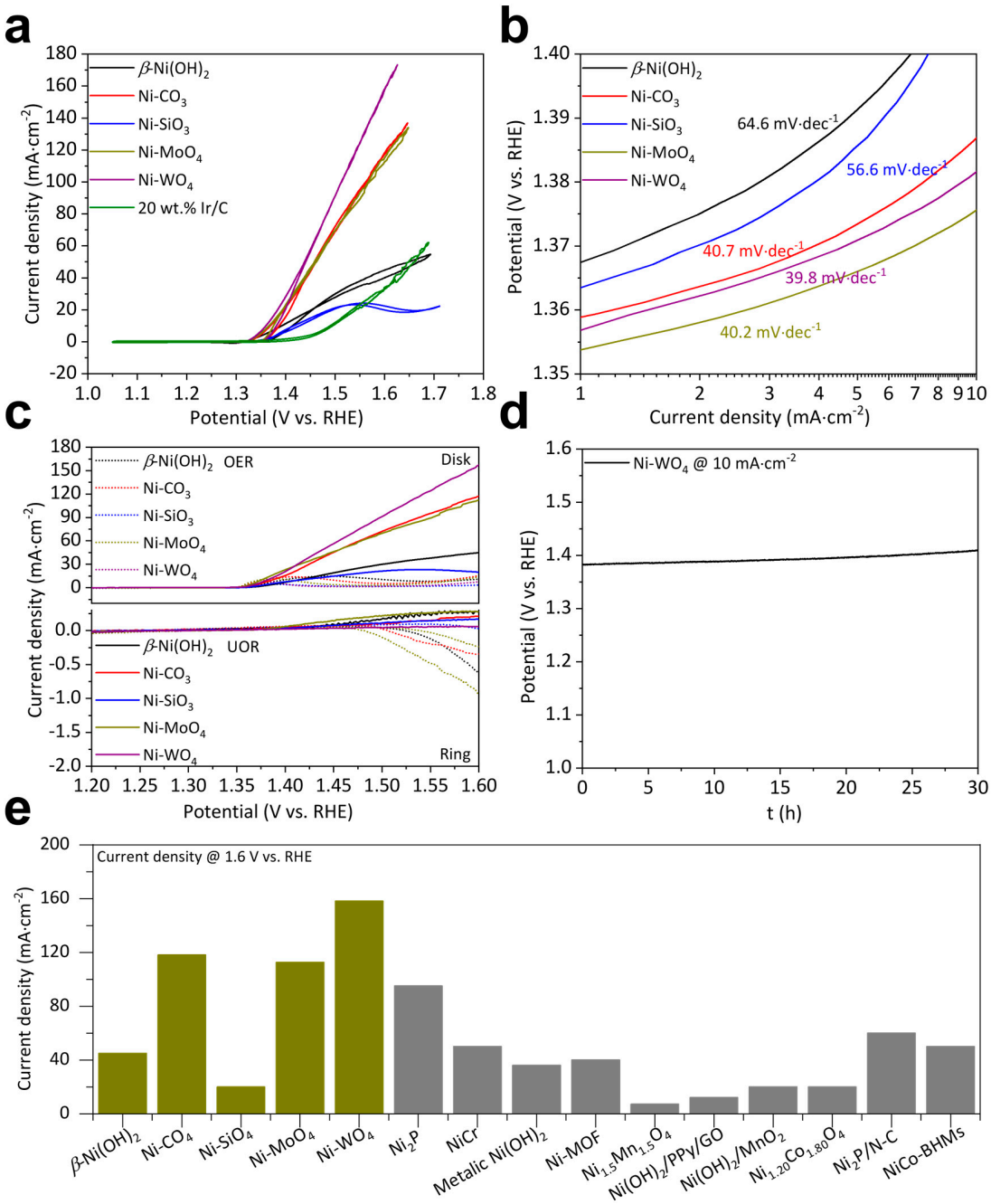


Figure 3. (**a**) UOR CV curves, (**b**) UOR Tafel slopes, and (**c**) OER and UOR RRDE polarization curves of β-Ni(OH)$_2$, Ni-CO_3, Ni-SiO_3, Ni-MoO_4, and Ni-WO_4. (**d**) UOR durability of Ni-WO_4. (**e**) Comparison of UOR performance of catalysts decorated on glassy carbon electrode.

2.3. Determining Factors of UOR Activity

Catalytic activity is the sum of activity per active site. Therefore, the activity per active site and the quantity of active sites co-determine the catalyst activity [49]. Charge transfer resistance reflecting the UOR barrier was evaluated by EIS [38]. The UOR EIS diameter follows this sequence: Ni-SiO_3 < β-Ni$(OH)_2$ < Ni-MoO_4 < Ni-CO_3 < Ni-WO_4 (Figure 4a), suggesting that the UOR process proceeds more efficiently on Ni-WO_4 than Ni-SiO_3, Ni-MoO_4, and Ni-CO_3.

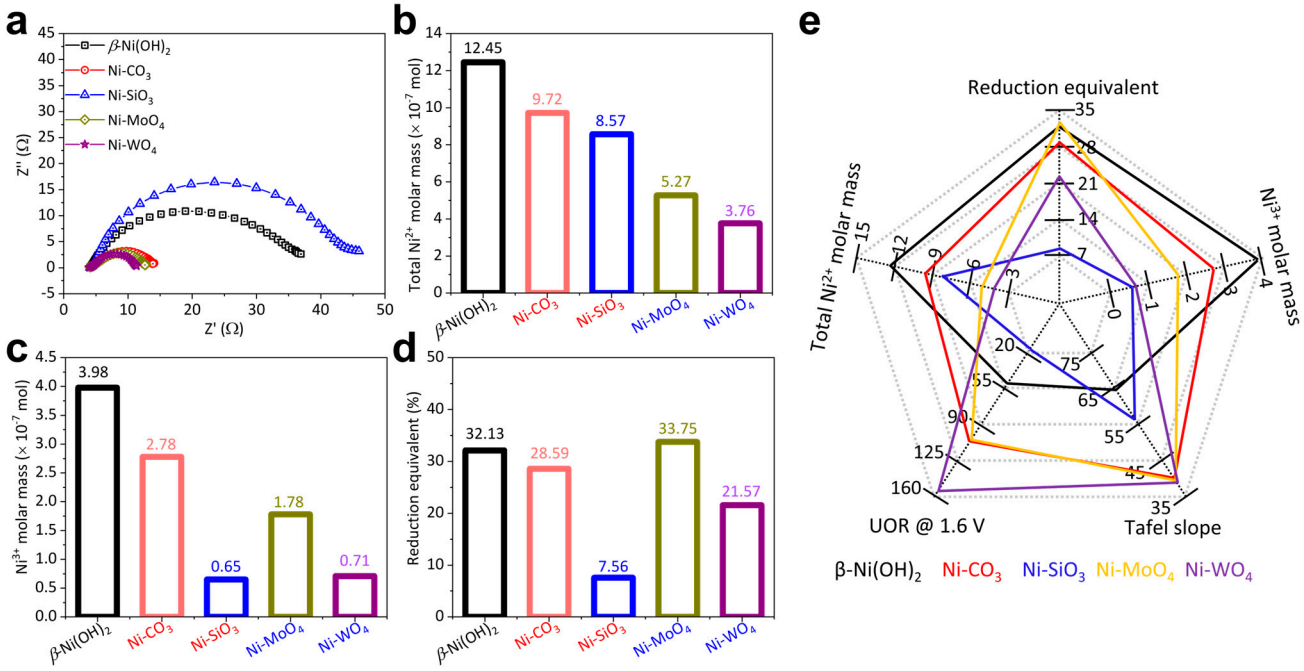


Figure 4. (**a**) UOR EIS, (**b**) total Ni^{2+} molar mass, (**c**) Ni^{3+} molar mass transformed from Ni^{2+}, (**d**) reduction equivalent, and (**e**) summary of UOR performance of β-Ni$(OH)_2$, Ni-CO_3, Ni-SiO_3, Ni-MoO_4, and Ni-WO_4.

The quantity of active sites: It is widely believed that Ni^{3+} moieties are the true active sites and the pre-catalysts just serve as the precursors during UOR catalysis [11,25,31,50]. It is crucial to untangle the relationship among the Ni^{2+} molar mass, the Ni^{3+} molar mass, the reduction equivalent (the capacity to accumulate Ni^{3+}) and UOR activity. The total Ni^{2+} molar mass (calculated from the catalyst loading on glass carbon electrode) follows this sequence: β-Ni$(OH)_2$ > Ni-CO_3 > Ni-SiO_3 > Ni-MoO_4 > Ni-WO_4 (Figure 4b). The Ni^{3+} molar mass (calculated from the reduction peak in Figure S4b) follows this sequence: β-Ni$(OH)_2$ > Ni-CO_3 > Ni-MoO_4 > Ni-WO_4 > Ni-SiO_3 (Figure 4c). The reduction equivalent follows this sequence: Ni-MoO_4 > β-Ni$(OH)_2$ > Ni-CO_3 > Ni-WO_4 > Ni-SiO_3 (Figure 4d). The summary of the relationship among the Ni^{2+} molar mass, the Ni^{3+} molar mass, reduction equivalent and UOR activity is shown in Figure 4e. The Ni^{2+} molar mass, Ni^{3+} molar mass, reduction equivalent and UOR activity do not exhibit a reasonable logic relationship, indicating that the quantity of active sites cannot solely decide the UOR activity.

The activity per active site: The activity per active site is determined by the electronic structure of catalysts. The electronic structure was analyzed by valence band (VB) spectra shown in Figure 5a. VB spectra of β-Ni$(OH)_2$, Ni-CO_3, and Ni-SiO_3 demonstrate similar shapes and are just located at slightly different binding energies. VB spectra of Ni-MoO_4 and Ni-WO_4 exhibit similar shapes but significantly differ from those of β-Ni$(OH)_2$, Ni-CO_3, and Ni-SiO_3 especially below 6 eV. This indicates that Ni-MoO_4 and Ni-WO_4 possess significantly different electronic structures from β-Ni$(OH)_2$, Ni-CO_3, and Ni-SiO_3 [7]. This phenomenon is due to the fact that transition metals mainly contribute below 6 eV in VB spectra [51]. D

band centers were calculated from VB spectra (Figure 5b). D band center positions follow this sequence: Ni-CO_3 (−4.78 eV) > β-Ni$(OH)_2$ (−4.81 eV) > Ni-SiO_3 (−4.89 eV) > Ni-MoO_4 (−5.46 eV) > Ni-WO_4 (−5.57 eV). The lower the d band center position, the weaker the bonding strength between the catalyst and intermediates. The bonding strength between the catalyst and intermediates subject to d band center position [51,52] and the bonding scheme are depicted in Figure 5c. The desorption of the UOR intermediates is the rate-controlling step and Ni-WO_4 demonstrates the lowest d band center, which facilitates the desorption of the UOR intermediates. Therefore, Ni-WO_4 exhibits the highest activity per active site. For the direct analysis of the activity per active site, the UOR CV curves were normalized by the Ni^{2+} and Ni^{3+} molar mass. The UOR activity per Ni^{2+} molar mass follows this sequence: β-Ni$(OH)_2$ ≈ Ni-CO_3 < Ni-SiO_3 < Ni-MoO_4 < Ni-WO_4 (Figure 5d). The UOR activity per Ni^{3+} molar mass follows this sequence: Ni-CO_3 < Ni-SiO_3 < β-Ni$(OH)_2$ < Ni-MoO_4 < Ni-WO_4 (Figure 5e). The summary of the total Ni^{2+} molar mass, Ni^{3+} molar mass, and UOR activity does not exhibit a reasonable logic relationship, suggesting that the activity per active site cannot solely determine the UOR activity as well (Figure 5f).

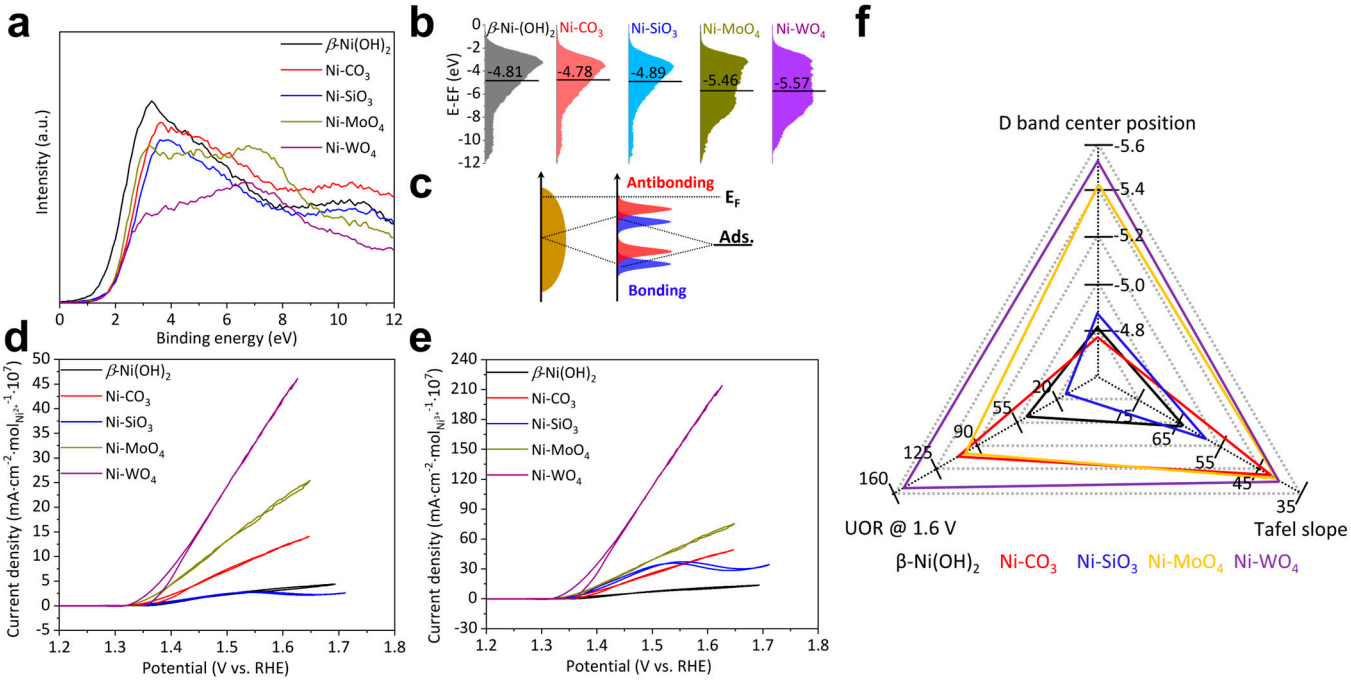


Figure 5. (**a**) Valence band spectra, (**b**) d band models derived from valence band spectra, (**c**) bond formation scheme, (**d**) UOR CV curves normalized by the total Ni^{2+} molar mass, (**e**) UOR CV curves normalized by Ni^{3+} molar mass, and (**f**) summary of UOR performance of β-Ni$(OH)_2$, Ni-CO_3, Ni-SiO_3, Ni-MoO_4, and Ni-WO_4.

The activity per active site and the quantity of active sites co-determines the UOR activity of β-Ni$(OH)_2$, Ni-CO_3, Ni-SiO_3, Ni-MoO_4, and Ni-WO_4. Ni-WO_4 with the lowest d band center position demonstrates the highest activity per active site and possesses slightly fewer active sites compared to Ni-CO_3 with the maximum quantity of active sites. Therefore, Ni-WO_4 exhibits the highest UOR activity.

2.4. Effect of the Pre-Catalyst Catalyst on UOR Activity

To verify if the true active sites are Ni^{3+} moieties for Ni-WO_4 and Ni-CO_3, TEM and XPS were adopted to examine Ni-WO_4 durability and Ni-CO_3 durability. Catalyst nanoparticles and Ketjen black are observed in TEM images of Ni-WO_4 durability and Ni-CO_3 durability (Figure 6a,c). HRTEM images of Ni-WO_4 durability and Ni-CO_3 durability both demonstrate a facet with a width of 2.08 Å ascribed to the (200) facet of nickel (oxy)hydroxide (Figure 6b,d) [22,35]. Ni $2p_{3/2}$ XPS of Ni-WO_4 durability and Ni-CO_3

durability are fitted with Ni^{2+} (856.10 eV) and Ni^{3+} (857.80 eV), followed by a satellite (862.70 eV) [36], confirming the formation of Ni^{3+} moieties. W 4f XPS of Ni-WO_4 possesses three peaks of $4f_{7/2}$ (34.98 eV), $4f_{5/2}$ (37.16 eV), and tungsten oxide loss feature (40.81 eV) (Figure 6f) [53,54]. W signal cannot be detected in the corresponding binding energy range for Ni-WO_4 durability, suggesting that element W on the Ni-WO_4 surface was completely dissolved during UOR catalysis. F 1s XPS of Ni-WO_4 durability demonstrates one peak of C-F moieties located at 35.39 eV which results from the Nafion molecules (Figure 6f) [55]. C-C (284.60 eV), C-O (286.14 eV), C=O (287.60 eV), C-O (289.29), and C=O (291.46) are detected in C 1s XPS of Ni-CO_3 (Figure 6g) [55,56]. C-C (284.60 eV), C-O (286.14 eV), C=O (287.60 eV), C-F (288.77 eV), -CF_2-CF_2-/-SCF_2-C- (292.19 eV), -OCF_2-C- (293.88 eV), and -CF_3-C- (296.89 eV) are detected in C 1s XPS of Ni-CO_3 durability (Figure 6g) [55]. The comparison of C 1s and W 4f fitting results of Ni-CO_3 and Ni-WO_4 before and after UOR durability tests (Table S1). The signal of nickel carbonate structure in C 1s XPS spectrum of Ni-CO_3 durability disappeared, indicating the complete dissolution of nickel carbonate on Ni-CO_3 surface during UOR catalysis. The UOR activity of both Ni-WO_4 and Ni-CO_3 just slightly fluctuates during the continuous 5000 cycles (Figure 6h,i). Therefore, we can infer that the WO_4^{2-} and CO_3^{2-} do not directly participate in the UOR catalysis and true active sites are Ni^{3+} moieties. The higher UOR activity of Ni-WO_4 than Ni-CO_3 for all the 5000 cycles indicates that the pre-catalysts are not the true active sites but determine the final UOR activity.

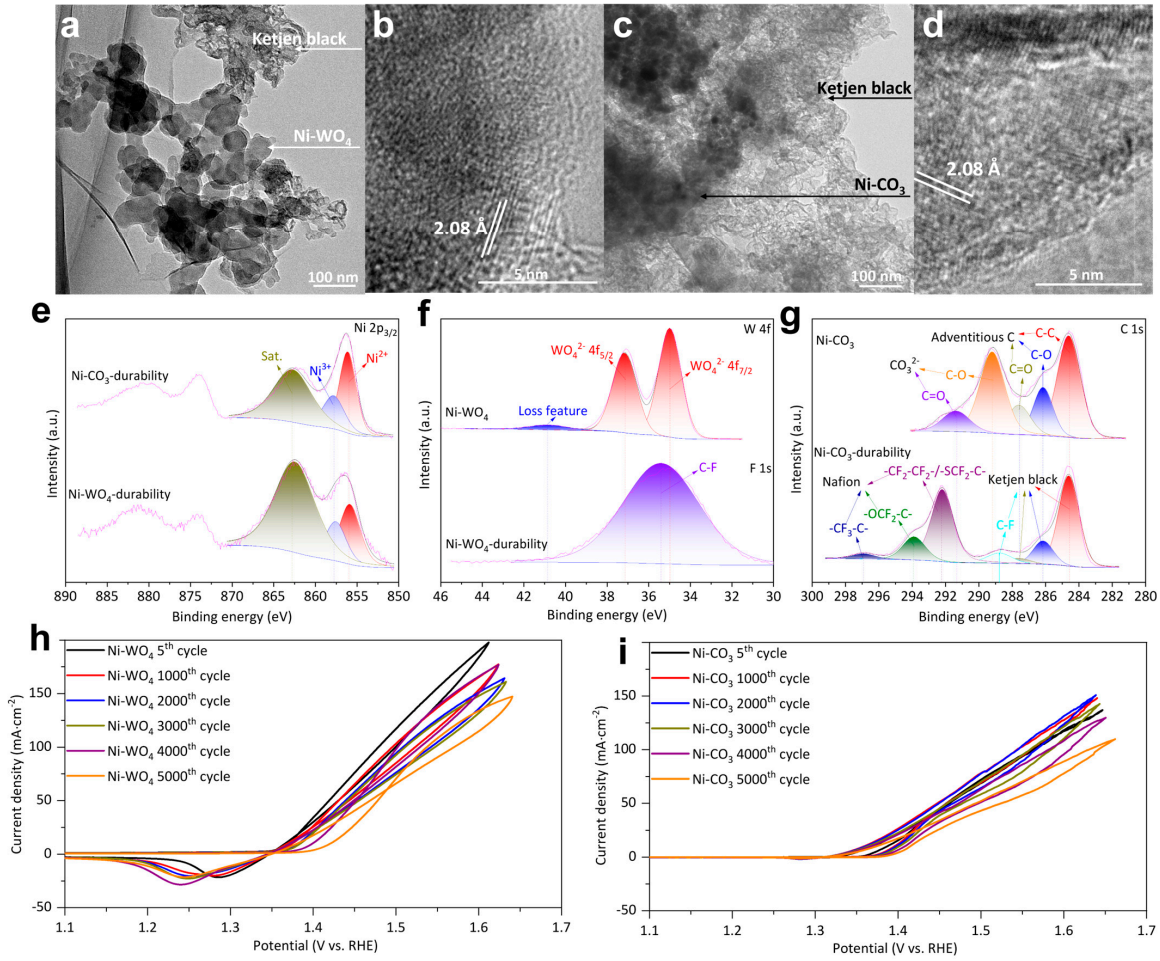


Figure 6. (**a**) TEM image and (**b**) HRTEM image of Ni-WO_4 durability. (**c**) TEM image and (**d**) HRTEM image of Ni-CO_3 durability. (**e**) Ni 2p XPS of Ni-CO_3 durability and Ni-WO_4 durability. (**f**) W 4f XPS of Ni-WO_4 and F 1s XPS of Ni-WO_4 durability. (**g**) C 1s XPS of Ni-CO_3 and Ni-CO_3 durability. (**h**) UOR CV curves of Ni-WO_4. (**i**) UOR CV curves of Ni-CO_3.

3. Materials and Methods

3.1. Fabrication of β-Ni(OH)$_2$, Ni-CO$_3$, Ni-SiO$_3$, Ni-MoO$_4$, and Ni-WO$_4$

1 M Ni^{2+}, OH^-, CO_3^{2-}, SiO_3^{2-}, MoO_4^{2-}, and WO_4^{2-} solutions were prepared by dispersing the salts of $NiCl_2 \cdot 6H_2O$, NaOH, Na_2CO_3, Na_2SiO_3, $Na_2MoO_4 \cdot 2H_2O$, and $Na_2WO_4 \cdot 2H_2O$ in deionized water, respectively. β-Ni(OH)$_2$ was obtained by mixing Ni^{2+} solution with OH^- solution with a volume ratio of 1:2. Ni-CO$_3$, Ni-SiO$_3$, Ni-MoO$_4$, and Ni-WO$_4$ were prepared by mixing Ni^{2+} solution with CO_3^{2-}, SiO_3^{2-}, MoO_4^{2-}, and WO_4^{2-} solutions with a volume ratio of 1:1, respectively. After being thoroughly washed, centrifugated, and lyophilized, β-Ni(OH)$_2$, Ni-CO$_3$, Ni-SiO$_3$, Ni-MoO$_4$, and Ni-WO$_4$ were obtained.

3.2. Structure Characterization

An X-ray diffractometer (XRD, DX–2700BH, Dandong Haoyuan instrument, Dandong, China) was used to collect XRD data with Cu K_α radiation at a scan rate of $2^\circ \cdot min^{-1}$. A transmission electron microscope (TEM, JEOL JEM–2100F, Japan Electronics Co., Ltd, Showima City, Tokyo, Japan) was used to observe catalysts' morphologies with an accelerating voltage of 200 kV. An X-ray photoelectron spectroscope (XPS, Axis Supra, Shimadzu, Japan) was used to analyze element chemical states. A Shirley background was applied to all the XPS spectra and binding energies of all XPS spectra were charge referenced to 284.8 eV. The equation $\int N(\varepsilon)\varepsilon d\varepsilon / \int N(\varepsilon) d\varepsilon$ was applied to calculate the d band center, where $N(\varepsilon)$ represents the density of states.

3.3. Electrochemcial Analysis

The UOR performance was evaluated in 1 M KOH with 0.33 M urea. The as-synthesized catalysts, a Hg/HgO electrode and a carbon rod, were used as the working, reference, and counter electrodes. Working electrodes were prepared by casting 30 μL catalyst inks onto a glass carbon electrode polished by a polishing cloth using 50 nm Al_2O_3. Catalysts (4 mg) and ketjen black (0.5 mg) dispersed into the mixed solution of ethanol (1000 μL) and Nafion (40 μL) were used as the catalyst ink. Cyclic voltammetry (CV) curves scanned at 5 $mV \cdot s^{-1}$, chronopotentiometry (CP) curves measured at 10 $mA \cdot cm^{-1}$, electrochemical impedance spectroscopy (EIS) tested at 1.4 V from 100 mHz to 100 kHz, and the rotating ring-disk electrode (RRDE) method were used to analyze the UOR performance. The electrochemical data were collected after 10 cycles of CV curves in 1 M KOH. All the potentials were calibrated by the equation $E_{RHE} = E_{Hg/HgO} + 0.098 + 0.059 \times pH$. The reduction equivalent was calculated by the equation $RE = n(Ni^{3+})/n(Ni^{2+})$.

4. Conclusions

In summary, β-Ni(OH)$_2$, Ni-CO$_3$, Ni-SiO$_3$, Ni-MoO$_4$, and Ni-WO$_4$ were fabricated by bonding Ni^{2+} with OH^-, CO_3^{2-}, SiO_3^{2-}, MoO_4^{2-}, and WO_4^{2-} anions, respectively. Through systematic investigations about the catalysts structure and UOR mechanism, the five as-fabricated catalysts are found to serve as pre-catalysts and the true active sites are the in situ-formed Ni^{3+} moieties. The pre-catalyst has effects on the quantity of active sites and the activity per active site to determine the UOR activity. The as-fabricated amorphous nickel tungstate possesses the most superior activity per active site and a relatively high number of active sites, thus demonstrating excellent UOR activity to catalyze the UOR reaching 158.10 $mA \cdot cm^{-2}$ at 1.6 V, exceeding the majority of the reported catalysts. This work provides a deeper understanding of the pre-catalyst effect on UOR activity.

Supplementary Materials: The following supporting information can be downloaded at: https://www.mdpi.com/article/10.3390/molecules29143321/s1, Figure S1: XRD patterns of β-Ni(OH)$_2$, Ni-CO_3, Ni-SiO_3, Ni-MoO_4 and Ni-WO_4; Figure S2: (a–d) TEM images of β-Ni(OH)$_2$, Ni-CO_3, Ni-SiO_3 and Ni-MoO_4. (e–h) HRTEM images of β-Ni(OH)$_2$, Ni-CO_3, Ni-SiO_3 and Ni-MoO_4, insets are the corresponding SAED patterns; Figure S3: (a) Si 2p XPS of Ni-SiO_3. (b) Mo 3d XPS of Ni-MoO_4; Figure S4: (a) OER and UOR CV curves of β-Ni(OH)$_2$, Ni-CO_3, Ni-SiO_3, Ni-MoO_4, Ni-WO_4 and 20 wt.% Ir/C. (b) OER CV curves of β-Ni(OH)$_2$, Ni-CO_3, Ni-SiO_3, Ni-MoO_4, Ni-WO_4 and 20 wt.% Ir/C; Table S1: C 1s and W 4f XPS fitting results of Ni-CO_3 and Ni-WO_4.

Author Contributions: Conceptualization, H.L. and L.C.; methodology, H.L.; software, P.W. and X.Q.; validation, H.L., L.C., S.Y. and J.W.; formal analysis, H.L., L.C., S.Y. and J.W.; investigation, A.Y., Y.W., Y.Y., J.L. and Z.R.; resources, H.L., L.C., S.Y. and J.W.; data curation, P.W. and X.Q.; writing—original draft preparation, H.L.; writing—review and editing, H.L., L.C., S.Y. and J.W.; visualization, H.L. and L.C.; supervision, L.C., S.Y. and J.W.; project administration, J.W.; funding acquisition, H.L. and J.W. All authors have read and agreed to the published version of the manuscript.

Funding: This research was funded by National Natural Science Foundation of China (52201257), Shenzhen Science and Technology Program (KQTD20200820113045083 and JCYJ20220818102403007), Newly Introduced Scientific Research Start-up Funds for High-tech Talents (DD11409024) and Shenzhen Research Fund for Returned Scholars (DD11409017 and AK29100016).

Institutional Review Board Statement: Not applicable.

Informed Consent Statement: Not applicable.

Data Availability Statement: The original contributions presented in the study are included in the article/Supplementary Material, further inquiries can be directed to the corresponding authors.

Conflicts of Interest: The authors declare no conflicts of interest.

References

1. Ren, L.; Yang, D.; Li, J.; Li, H.; Yang, J.-H. Nitrogen doped carbon fiber supported nickel phosphide for efficient electrocatalytic overall urea splitting. *Appl. Surf. Sci.* **2023**, *624*, 157173. [CrossRef]
2. Wei, T.; Meng, G.; Zhou, Y.; Wang, Z.; Liu, Q.; Luo, J.; Liu, X. Amorphous Fe-Co oxide as an active and durable bifunctional catalyst for the urea-assisted H_2 evolution reaction in seawater. *Chem. Commun.* **2023**, *59*, 9992–9995. [CrossRef]
3. Xu, X.; Xu, L.; Wei, X.; Huang, M.; Toghan, A. Unravelling the mechanistic pathway of the Ni_5P_4/NiSe heterojunction for catalyzing the urea-rich water oxidation. *Mater. Today Phys.* **2023**, *36*, 101148. [CrossRef]
4. Soltani, M.; Amin, H.M.A.; Cebe, A.; Ayata, S.; Baltruschat, H. Metal-Supported Perovskite as an Efficient Bifunctional Electrocatalyst for Oxygen Reduction and Evolution: Substrate Effect. *J. Electrochem. Soc.* **2021**, *168*, 034504. [CrossRef]
5. Saeed, M.; Munir, M.; Intisar, A.; Waseem, A. Facile Synthesis of a Novel Ni-WO_3@g-C_3N_4 Nanocomposite for Efficient Oxidative Desulfurization of Both Model and Real Fuel. *ACS Omega* **2022**, *7*, 15809–15820. [CrossRef] [PubMed]
6. Liu, Z.; Amin, H.M.A.; Peng, Y.; Corva, M.; Pentcheva, R.; Tschulik, K. Facet-Dependent Intrinsic Activity of Single Co_3O_4 Nanoparticles for Oxygen Evolution Reaction. *Adv. Funct. Mater.* **2022**, *33*, 2210945. [CrossRef]
7. Wang, L.; Zhu, Y.; Wen, Y.; Li, S.; Cui, C.; Ni, F.; Liu, Y.; Lin, H.; Li, Y.; Peng, H.; et al. Regulating the Local Charge Distribution of Ni Active Sites for the Urea Oxidation Reaction. *Angew. Chem. Int. Ed. Engl.* **2021**, *60*, 10577–10582. [CrossRef] [PubMed]
8. Gan, Y.; Ye, Y.; Dai, X.; Yin, X.; Cao, Y.; Cai, R.; Feng, B.; Wang, Q.; Zhang, X. La and S Co-Doping Induced the Synergism of Multiphase Nickel-Iron Nanosheets with Rich Oxygen Vacancies to Trigger Large-Current-Density Oxygen Evolution and Urea Oxidation Reactions. *Small* **2023**, *19*, e2303250. [CrossRef]
9. Kim, M.; Min, K.; Ko, D.; Seong, H.; Eun Shim, S.; Baeck, S.H. Regulating the electronic structure of Ni_2P by one-step Co, N dual-doping for boosting electrocatalytic performance toward oxygen evolution reaction and urea oxidation reaction. *J. Colloid Interface Sci.* **2023**, *650 Pt B*, 1851–1861. [CrossRef]
10. Li, P.; Li, W.; Huang, Y.; Huang, Q.; Li, F.; Tian, S. Surface Engineering over Metal-Organic Framework Nanoarray to Realize Boosted and Sustained Urea Oxidation. *Small* **2023**, *19*, e2305585. [CrossRef]
11. Liao, Y.; Chen, Y.; Li, L.; Luo, S.; Qing, Y.; Tian, C.; Xu, H.; Zhang, J.; Wu, Y. Ultrafine Homologous Ni_2P–Co_2P Heterostructures via Space-Confined Topological Transformation for Superior Urea Electrolysis. *Adv. Funct. Mater.* **2023**, *33*, 2303300. [CrossRef]
12. Liu, X.; Lu, H.; Zhu, S.; Cui, Z.; Li, Z.; Wu, S.; Xu, W.; Liang, Y.; Long, G.; Jiang, H. Alloying-Triggered Phase Engineering of NiFe System via Laser-Assisted Al Incorporation for Full Water Splitting. *Angew. Chem. Int. Ed. Engl.* **2023**, *62*, e202300800. [CrossRef]
13. Zhang, K.; Guo, F.; Graham, N.; Yu, W. Engineering Morphology and Electron Redistribution of a Ni/WO_3 Mott-Schottky Bifunctional Electrocatalyst for Efficient Alkaline Urea Splitting. *ACS Appl. Mater. Interfaces* **2023**, *15*, 50116–50125. [CrossRef]

14. Zan, L.; Amin, H.M.A.; Mostafa, E.; Abd-El-Latif, A.A.; Iqbal, S.; Baltruschat, H. Electrodeposited Cobalt Nanosheets on Smooth Silver as a Bifunctional Catalyst for OER and ORR: In Situ Structural and Catalytic Characterization. *ACS Appl. Mater. Interfaces* **2022**, *14*, 55458–55470. [CrossRef]
15. Liu, Z.; Corva, M.; Amin, H.M.A.; Blanc, N.; Linnemann, J.; Tschulik, K. Single Co_3O_4 Nanocubes Electrocatalyzing the Oxygen Evolution Reaction: Nano-Impact Insights into Intrinsic Activity and Support Effects. *Int. J. Mol. Sci.* **2021**, *22*, 13137. [CrossRef]
16. Veettil, V.T.; Vijayakumar, A.U.; Ashdot, A.; Zitoun, D. Precious-Group-Metal-Free Energy-Efficient Urea Electrolysis: Membrane Electrode Assembly Cell Using Ni_3N Nanoparticles as Catalyst. *ACS Appl. Energy Mater.* **2022**, *5*, 1397–1402. [CrossRef]
17. Wang, X.-H.; Hong, Q.-L.; Zhang, Z.-N.; Ge, Z.-X.; Zhai, Q.-G.; Jiang, Y.-C.; Chen, Y.; Li, S.-N. Two-dimensional nickel–cobalt bimetallic hydroxides towards urea electrooxidation. *Appl. Surf. Sci.* **2022**, *604*, 154484. [CrossRef]
18. Zhang, X.; Ma, G.; Shui, L.; Zhou, G.; Wang, X. Urea electrooxidation-boosted hydrogen production on nitrogen-doped porous carbon nanorod-supported nickel phosphide nanoparticles. *J. Energy Chem.* **2022**, *72*, 88–96. [CrossRef]
19. Zhao, Z.; Wang, H.; Tan, H.; Wu, X.; Kang, Y.; Dong, Y.; Li, X.; Jin, S.; Chang, X. Deciphering the active origin for urea oxidation reaction over nitrogen penetrated nickel nanoparticles embedded in carbon nanotubes. *J. Colloid Interface Sci.* **2022**, *626*, 740–751. [CrossRef] [PubMed]
20. Zhu, D.; Zhang, H.; Miao, J.; Hu, F.; Wang, L.; Tang, Y.; Qiao, M.; Guo, C. Strategies for designing more efficient electrocatalysts towards the urea oxidation reaction. *J. Mater. Chem. A* **2022**, *10*, 3296–3313. [CrossRef]
21. Chang, J.; Lv, Q.; Li, G.; Ge, J.; Liu, C.; Xing, W. Core-shell structured $Ni_{12}P_5/Ni_3(PO_4)_2$ hollow spheres as difunctional and efficient electrocatalysts for overall water electrolysis. *Appl. Catal. B-Environ.* **2017**, *204*, 486–496. [CrossRef]
22. He, M.; Feng, C.; Liao, T.; Hu, S.; Wu, H.; Sun, Z. Low-Cost $Ni_2P/Ni_{0.96}S$ Heterostructured Bifunctional Electrocatalyst toward Highly Efficient Overall Urea-Water Electrolysis. *ACS Appl. Mater. Interfaces* **2020**, *12*, 2225–2233. [CrossRef] [PubMed]
23. Hu, S.; Wang, S.; Feng, C.; Wu, H.; Zhang, J.; Mei, H. Novel MOF-Derived Nickel Nitride as High-Performance Bifunctional Electrocatalysts for Hydrogen Evolution and Urea Oxidation. *ACS Sustain. Chem. Eng.* **2020**, *8*, 7414–7422. [CrossRef]
24. Li, Y.; Jiang, H.; Cui, Z.; Zhu, S.; Li, Z.; Wu, S.; Ma, L.; Han, X.; Liang, Y. Spin State Tuning of the Octahedral Sites in Ni–Co-Based Spinel toward Highly Efficient Urea Oxidation Reaction. *J. Phys. Chem. C* **2021**, *125*, 9190–9199. [CrossRef]
25. Liu, H.; Zhu, S.; Cui, Z.; Li, Z.; Wu, S.; Liang, Y. Ni_2P nanoflakes for the high-performing urea oxidation reaction: Linking active sites to a UOR mechanism. *Nanoscale* **2021**, *13*, 1759–1769. [CrossRef] [PubMed]
26. Meng, J.; Chernev, P.; Mohammadi, M.R.; Klingan, K.; Loos, S.; Pasquini, C.; Kubella, P.; Jiang, S.; Yang, X.; Cui, Z.; et al. Self-supported $Ni(OH)_2/MnO_2$ on CFP as a flexible anode towards electrocatalytic urea conversion: The role of composition on activity, redox states and reaction dynamics. *Electrochim. Acta* **2019**, *318*, 32–41. [CrossRef]
27. Ma, G.; Xue, Q.; Zhu, J.; Zhang, X.; Wang, X.; Yao, H.; Zhou, G.; Chen, Y. Ultrafine Rh nanocrystals decorated ultrathin NiO nanosheets for urea electro-oxidation. *Appl. Catal. B-Environ.* **2020**, *265*, 118567. [CrossRef]
28. Yang, J.-H.; Chen, M.; Xu, X.; Jiang, S.; Zhang, Y.; Wang, Y.; Li, Y.; Zhang, J.; Yang, D. CuO-$Ni(OH)_2$ nanosheets as effective electro-catalysts for urea oxidation. *Appl. Surf. Sci.* **2021**, *560*, 150009. [CrossRef]
29. Chen, F.; Yang, F.; Sheng, C.; Li, J.; Xu, H.; Qing, Y.; Chen, S.; Wu, Y.; Lu, X. Electronic structure modulation of nickel hydroxide porous nanowire arrays via manganese doping for urea-assisted energy-efficient hydrogen generation. *J. Colloid Interface Sci.* **2022**, *626*, 445–452. [CrossRef]
30. Yang, W.; Yang, X.; Hou, C.; Li, B.; Gao, H.; Lin, J.; Luo, X. Rapid room-temperature fabrication of ultrathin $Ni(OH)_2$ nanoflakes with abundant edge sites for efficient urea oxidation. *Appl. Catal. B-Environ.* **2019**, *259*, 118020. [CrossRef]
31. Hu, S.; Feng, C.; Wang, S.; Liu, J.; Wu, H.; Zhang, L.; Zhang, J. Ni_3N/NF as Bifunctional Catalysts for Both Hydrogen Generation and Urea Decomposition. *ACS Appl. Mater. Interfaces* **2019**, *11*, 13168–13175. [CrossRef] [PubMed]
32. Cao, Z.; Mao, H.; Guo, X.; Sun, D.; Sun, Z.; Wang, B.; Zhang, Y.; Song, X.-M. Hierarchical $Ni(OH)_2$/Polypyrrole/Graphene Oxide Nanosheets as Excellent Electrocatalysts for the Oxidation of Urea. *ACS Sustain. Chem. Eng.* **2018**, *6*, 15570–15581. [CrossRef]
33. Abdel Hameed, R.M.; Medany, S.S. NiO nanoparticles on graphene nanosheets at different calcination temperatures as effective electrocatalysts for urea electro-oxidation in alkaline medium. *J. Colloid Interface Sci.* **2017**, *508*, 291–302. [CrossRef] [PubMed]
34. Stoch, J.; Gablankowska-Kukucz, J. The Effect of Carbonate Contaminations on the XPS O 1s Band Structure in Metal Oxides. *Surf. Interface Anal.* **1991**, *17*, 165–167. [CrossRef]
35. Barwe, S.; Weidner, J.; Cychy, S.; Morales, D.M.; Dieckhofer, S.; Hiltrop, D.; Masa, J.; Muhler, M.; Schuhmann, W. Electrocatalytic Oxidation of 5-(Hydroxymethyl)furfural Using High-Surface-Area Nickel Boride. *Angew. Chem. Int. Ed. Engl.* **2018**, *57*, 11460–11464. [CrossRef] [PubMed]
36. Zhang, N.; Zou, Y.; Tao, L.; Chen, W.; Zhou, L.; Liu, Z.; Zhou, B.; Huang, G.; Lin, H.; Wang, S. Electrochemical Oxidation of 5-Hydroxymethylfurfural on Nickel Nitride/Carbon Nanosheets: Reaction Pathway Determined by In Situ Sum Frequency Generation Vibrational Spectroscopy. *Angew. Chem. Int. Ed. Engl.* **2019**, *58*, 15895–15903. [CrossRef] [PubMed]
37. Amin, H.M.A.; Attia, M.; Tetzlaff, D.; Apfel, U.P. Tailoring the Electrocatalytic Activity of Pentlandite $Fe_xNi_{9-x}S_8$ Nanoparticles via Variation of the Fe:Ni Ratio for Enhanced Water Oxidation. *ChemElectroChem* **2021**, *8*, 3863–3874. [CrossRef]
38. Guo, F.; Ye, K.; Du, M.; Huang, X.; Cheng, K.; Wang, G.; Cao, D. Electrochemical impedance analysis of urea electro-oxidation mechanism on nickel catalyst in alkaline medium. *Electrochim. Acta* **2016**, *210*, 474–482. [CrossRef]
39. Ni, M.; Ratner, B.D. Differentiation of Calcium Carbonate Polymorphs by Surface Analysis Techniques—An XPS and TOF-SIMS study. *Surf. Interface Anal.* **2008**, *40*, 1356–1361. [CrossRef]

40. Buchner, S.; Radtke, C.; Balzaretti, N.M. Densification of Lithium Disilicate under High Pressure Investigated by XPS. *Open J. Inorg. Non-Met. Mater.* **2013**, *3*, 15–21. [CrossRef]
41. Nesbitt, H.W.; Bancroft, G.M.; Henderson, G.S.; Ho, R.; Dalby, K.N.; Huang, Y.; Yan, Z. Bridging, non-bridging and free (O^{2-}) oxygen in Na_2O-SiO_2 glasses: An X-ray Photoelectron Spectroscopic (XPS) and Nuclear Magnetic Resonance (NMR) study. *J. Non-Cryst. Solids* **2011**, *357*, 170–180. [CrossRef]
42. Yao, J.; Zhou, Y.; Yan, J.M.; Jiang, Q. Regulating $Fe_2(MoO_4)_3$ by Au Nanoparticles for Efficient N_2 Electroreduction under Ambient Conditions. *Adv. Energy Mater.* **2021**, *11*, 2003701. [CrossRef]
43. Xie, F.Y.; Gong, L.; Liu, X.; Tao, Y.T.; Zhang, W.H.; Chen, S.H.; Meng, H.; Chen, J. XPS studies on surface reduction of tungsten oxide nanowire film by Ar^+ bombardment. *J. Electron Spectrosc. Relat. Phenom.* **2012**, *185*, 112–118. [CrossRef]
44. Haetge, J.; Djerdj, I.; Brezesinski, T. Nanocrystalline $NiMoO_4$ with an ordered mesoporous morphology as potential material for rechargeable thin film lithium batteries. *Chem. Commun.* **2012**, *48*, 6726–6728. [CrossRef] [PubMed]
45. Periyasamy, S.; Subramanian, P.; Levi, E.; Aurbach, D.; Gedanken, A.; Schechter, A. Exceptionally Active and Stable Spinel Nickel Manganese Oxide Electrocatalysts for Urea Oxidation Reaction. *ACS Appl. Mater. Interfaces* **2016**, *8*, 12176–12185. [CrossRef]
46. Singh, R.K.; Schechter, A. Electroactivity of NiCr Catalysts for Urea Oxidation in Alkaline Electrolyte. *ChemCatChem* **2017**, *9*, 3374–3379. [CrossRef]
47. Zhu, D.; Guo, C.; Liu, J.; Wang, L.; Du, Y.; Qiao, S.Z. Two-dimensional metal-organic frameworks with high oxidation states for efficient electrocatalytic urea oxidation. *Chem. Commun.* **2017**, *53*, 10906–10909. [CrossRef] [PubMed]
48. Zhu, X.; Dou, X.; Dai, J.; An, X.; Guo, Y.; Zhang, L.; Tao, S.; Zhao, J.; Chu, W.; Zeng, X.C.; et al. Metallic Nickel Hydroxide Nanosheets Give Superior Electrocatalytic Oxidation of Urea for Fuel Cells. *Angew. Chem. Int. Ed. Engl.* **2016**, *55*, 12465–12469. [CrossRef] [PubMed]
49. Seh, Z.W.; Kibsgaard, J.; Dickens, C.F.; Chorkendorff, I.; Norskov, J.K.; Jaramillo, T.F. Combining theory and experiment in electrocatalysis: Insights into materials design. *Science* **2017**, *355*, eaad4998. [CrossRef]
50. Wygant, B.R.; Kawashima, K.; Mullins, C.B. Catalyst or Precatalyst? The Effect of Oxidation on Transition Metal Carbide, Pnictide, and Chalcogenide Oxygen Evolution Catalysts. *ACS Energy Lett.* **2018**, *3*, 2956–2966. [CrossRef]
51. Zhou, Y.; Zhou, Z.; Shen, R.; Ma, R.; Liu, Q.; Cao, G.; Wang, J. Correlating electrocatalytic oxygen reduction activity with d-band centers of metallic nanoparticles. *Energy Storage Mater.* **2018**, *13*, 189–198. [CrossRef]
52. Chen, Z.; Song, Y.; Cai, J.; Zheng, X.; Han, D.; Wu, Y.; Zang, Y.; Niu, S.; Liu, Y.; Zhu, J.; et al. Tailoring the d-Band Centers Enables Co_4-N Nanosheets to Be Highly Active for Hydrogen Evolution Catalysis. *Angew. Chem. Int. Ed. Engl.* **2018**, *57*, 5076–5080. [CrossRef]
53. Babar, P.; Patil, K.; Lee, D.M.; Karade, V.; Gour, K.; Pawar, S.; Kim, J.H. Cost-effective and efficient water and urea oxidation catalysis using nickel-iron oxyhydroxide nanosheets synthesized by an ultrafast method. *J. Colloid Interface Sci.* **2021**, *584*, 760–769. [CrossRef] [PubMed]
54. Niu, L.; Li, Z.; Xu, Y.; Sun, J.; Hong, W.; Liu, X.; Wang, J.; Yang, S. Simple synthesis of amorphous $NiWO_4$ nanostructure and its application as a novel cathode material for asymmetric supercapacitors. *ACS Appl. Mater. Interfaces* **2013**, *5*, 8044–8052. [CrossRef] [PubMed]
55. Vijayakumar, M.; Bhuvaneswari, M.S.; Nachimuthu, P.; Schwenzer, B.; Kim, S.; Yang, Z.; Liu, J.; Graff, G.L.; Thevuthasan, S.; Hu, J. Spectroscopic investigations of the fouling process on Nafion membranes in vanadium redox flow batteries. *J. Membr. Sci.* **2011**, *366*, 325–334. [CrossRef]
56. Jia, Y.; Luo, T.; Yu, X.-Y.; Liu, J.-H.; Huang, X.-J. Surfactant-free preparation of nickel carbonate hydroxide in aqueous solution and its toxic ion-exchange properties. *New J. Chem.* **2013**, *37*, 534–539. [CrossRef]

Disclaimer/Publisher's Note: The statements, opinions and data contained in all publications are solely those of the individual author(s) and contributor(s) and not of MDPI and/or the editor(s). MDPI and/or the editor(s) disclaim responsibility for any injury to people or property resulting from any ideas, methods, instructions or products referred to in the content.